nature water

Article

https://doi.org/10.1038/s44221-022-00010-3

Nanovehicle-assisted monomer shuttling enables highly permeable and selective nanofiltration membranes for water purification

Received: 17 May 2022

Accepted: 28 November 2022

Published online: 27 February 2023

Check for updates

Ruobin Dai[1], Huimin Zhou[1], Tianlin Wang[1], Zhiwei Qiu[1], Li Long[2], Shihong Lin[3] ✉, Chuyang Y. Tang[2] ✉ & Zhiwei Wang[1] ✉

Fabricating nanofiltration membranes with high water permeance and selectivity is crucial to efficient water purification. However, achieving such a goal with a simple and cost-effective approach that is compatible with existing membrane manufacturing infrastructure remains a substantial technical challenge. Here we show a strategy of nanoemulsion-regulated interfacial polymerization (NERIP) based on nanovehicle-assisted monomer shuttling for fabricating highly permeable and selective nanofiltration membranes. In NERIP, the nanovehicles, which are surfactant-stabilized oil droplets (in water) enriched with piperazine (PIP), enter and merge into the hexane phase to initiate the polymerization between PIP and trimesoyl chloride. This nanovehicle-assisted monomer shuttling results in the formation of polyamide 'bubbles' that later collapse into nanocraters. The nanocrater structure substantially increases the surface area and void fraction of the polyamide layer. The PIP shuttling also accelerates the polymerization reaction, enabling the formation of a thin and highly cross-linked polyamide layer with a more uniform pore size distribution. These structural superiorities yield an unprecedentedly high performance with a water permeance of 36.8 ± 1.9 l m^{-2} h^{-1} bar^{-1} and a Na_2SO_4 rejection of 99.6 ± 0.1%. NERIP creates a new dimension to fabricate highly permeable and selective nanofiltration membranes for desalination and water purification.

Augmenting water supply from unconventional water sources including seawater, brackish water and even wastewater is critical for addressing global challenge of water scarcity[1–3]. Nanofiltration (NF), which can selectively remove multivalent salts and organic molecules with a molecular weight cutoff larger than 200 Da (refs. 4,5), has been regarded as an effective solution to achieve sustainable management of water resources[6–8]. When high rejection of monovalent ions is not required, NF is more efficient than reverse osmosis as it enables faster

[1]State Key Laboratory of Pollution Control and Resource Reuse, Shanghai Institute of Pollution Control and Ecological Security, School of Environmental Science and Engineering, Tongji University, Shanghai, China. [2]Department of Civil Engineering, The University of Hong Kong, Hong Kong, China. [3]Department of Civil and Environmental Engineering, Vanderbilt University, Nashville, TN, USA. ✉e-mail: shihong.lin@vanderbilt.edu; tangc@hku.hk; zwwang@tongji.edu.cn

https://doi.org/10.1038/s44221-022-00010-3

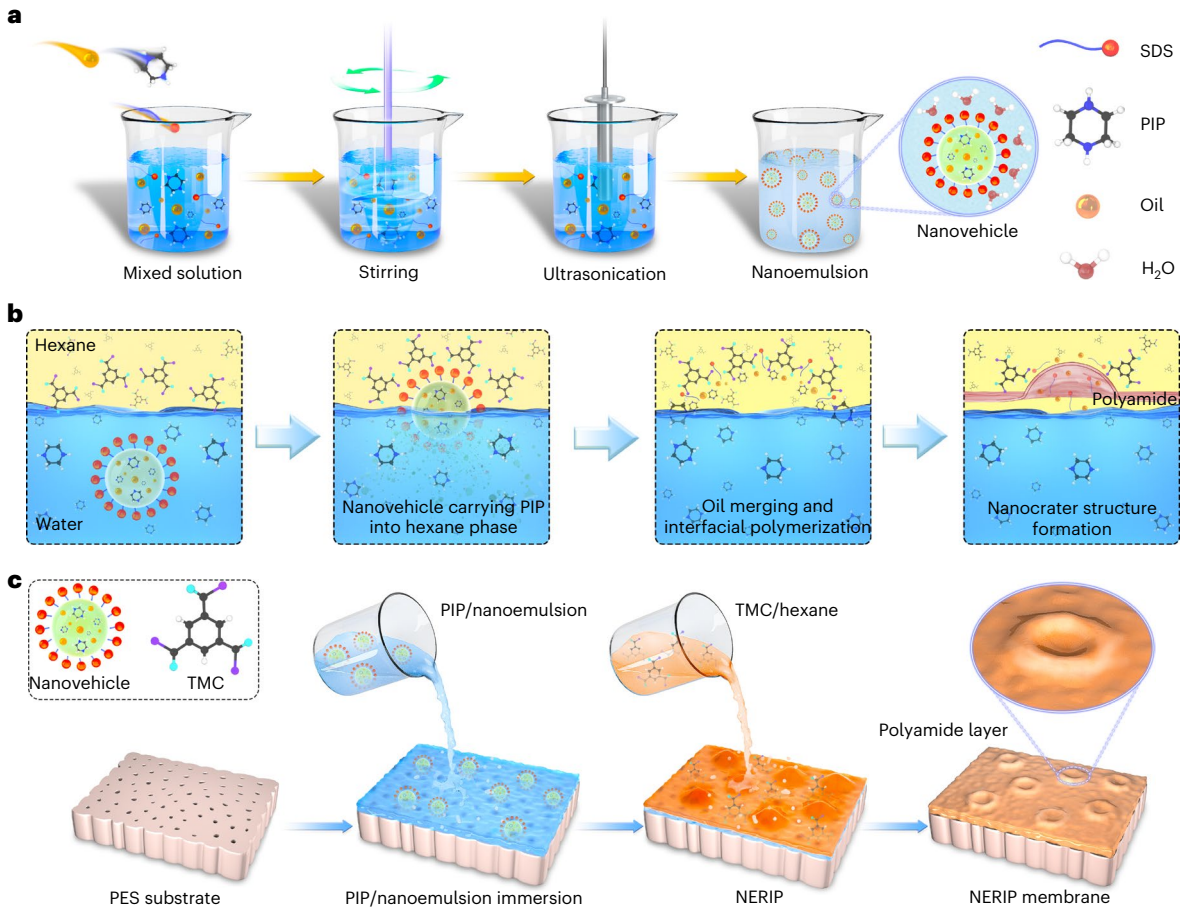

Fig. 1 | PA NF membrane fabrication based on NERIP. a, Preparation procedure of nanoemulsion containing nanovehicles with concentrated PIP monomers. PIP, oil and SDS were first dissolved in pure water. After being stirred, the mixed solution was subjected to ultrasonication to form the nanoemulsion. **b**, Schematic illustration of nanovehicle-assisted monomer shuttling for creation of the nanocrater structure of the PA active layer. The nanovehicle rapidly carries concentrated PIP across the water–hexane interface, and the nanovehicle merges into the hexane phase, exposing the PIP concentrated domain for reaction with TMC and finally forming a nanocrater-structured PA layer. **c**, Fabrication of a PA NF membrane based on NERIP. The PES ultrafiltration substrate was wetted by the nanoemulsion containing nanovehicles with concentrated PIP, followed by IP with TMC in hexane, to form the NERIP membrane with nanocrater structure.

water production with a lower pressure (water permeance typically >6 l m^{-2} h^{-1} bar^{-1} for NF)[9–11]. Most NF membranes are thin film composite (TFC) polyamide (PA) membranes[12] fabricated using interfacial polymerization (IP) with amine and acyl chloride monomers to form a PA active layer on a mesoporous support[13–15]. However, the performance of current TFC-PA NF membranes is constrained by the permeability–selectivity trade-off[9,10,16] due to the intrinsic morphology and structure of the PA separation layer. Synthesizing an NF membrane with exceedingly high permeance and selectivity can further improve the efficiency of NF-based separation[2,17,18].

Conventional IP (CIP) with piperazine (PIP) often generates a PA layer with a relatively low surface area and void fraction, which strongly limits the water permeance of the resulting TFC-PA membrane[19,20]. The PA layer from CIP may also suffer from a non-uniform pore size distribution, which constrains both the selectivity and ability of precise separation by NF[15,21]. To date, extensive efforts have been dedicated to improving the water permeance of TFC-PA membranes, such as inducing diffusion-driven instability during IP[19], incorporating hydrophilic additives during IP[22,23], modifying the surface of substrates[24,25] and using pre-loaded nanomaterials as templates[20]. However, few of these strategies can enhance the water permeance and improve selectivity simultaneously. Moreover, they require substantial modification of the existing procedure of manufacturing TFC-PA membranes and thus create extra hurdles for adoption and implementation at a large scale. Therefore, simultaneously enhancing the permeance and selectivity of TFC-PA NF membranes with a simple and cost-effective approach that is compatible with existing manufacturing infrastructure remains a substantial technical challenge.

Here, we report a facile and highly practical strategy of nanovehicle-assisted monomer shuttling during IP to dramatically increase the water permeance of the resulting TFC-PA NF membranes with a simultaneous enhancement in selectivity. The nanovehicles are surfactant-stabilized oil-in-water emulsions containing the PIP monomers, which have a markedly higher concentration in the emulsion than in bulk water (Fig. 1a). In the IP process, the concentrated PIP monomers were rapidly carried into the hexane phase by the nanovehicles (Fig. 1b), followed by a local, intensified reaction with trimesoyl chloride (TMC). This process, named nanoemulsion-regulated IP (NERIP), enabled the formation of TFC-PA membranes with nanocrater structures (Fig. 1c). The nanocrater structure of the NERIP membrane substantially increased the surface area and void fraction of the PA layer, resulting in an unprecedentedly high performance with a water permeance of 36.8 ± 1.9 l m^{-2} h^{-1} bar^{-1} and a Na_2SO_4 rejection of 99.6 ± 0.1%. Simultaneously, the NERIP membrane achieved a more uniform pore size distribution, which is important for more precise solute separations. The introduction of an additional liquid phase into water phase for IP reaction provides a new dimension for manipulating the properties and performance of TFC-PA membranes, which creates vast opportunities for enhancing the performance of TFC-PA membranes beyond the state-of-the-art.

https://doi.org/10.1038/s44221-022-00010-3

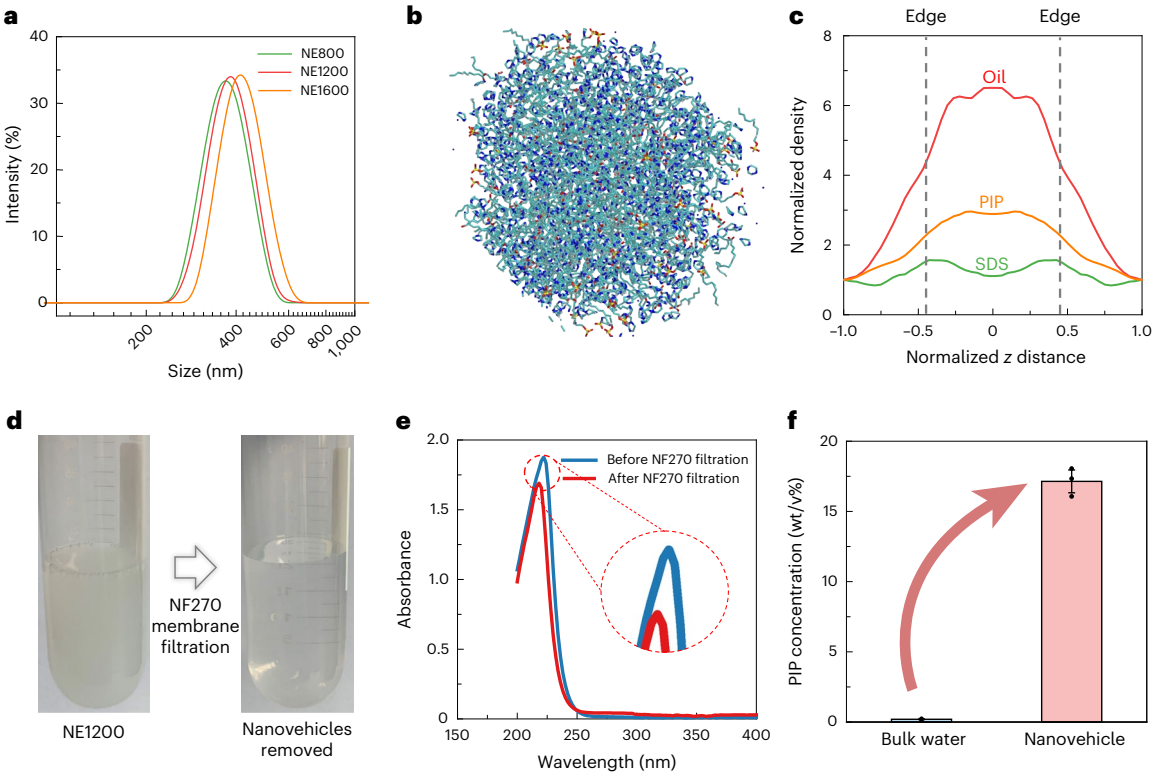

Fig. 2 | Formation and property of nanovehicles prepared by PIP, oil and SDS. **a**, Particle size distribution of nanodroplets, or nanovehicles, in nanoemulsion determined by dynamic light scattering. **b**, MD simulated structure of one nanodroplet in emulsion after self-assembly (water molecules are hidden). **c**, Distribution of PIP, oil and SDS in one nanovehicle along the normalized *z* distance obtained by MD simulation. **d**, Photographs of nanoemulsion NE1200 before and after NF270 membrane filtration. The nanoemulsion after the filtration showed complete removal of nanovehicles. **e**, Ultraviolet–visible curves of nanoemulsion NE1200 before and after NF270 membrane filtration. **f**, PIP concentrations in the bulk water and the nanovehicle for the NE1200 solution. The PIP concentration in the nanovehicle was calculated from the ultraviolet–visible curves of NE1200 before and after NF270 membrane filtration. Error bars in **f** represent the s.d. ($n = 3$) and data are presented as mean values ± s.d.

Creation of nanovehicle for rapid transport of aqueous monomers

The key to achieve rapid transport of aqueous monomers for regulating PA structure is to create nanoscale emulsified oil droplets as nanovehicles to carry PIP. Here, a nanoemulsion was prepared by stirring and ultrasonicating a mixture of PIP, oil and sodium dodecyl sulfate (SDS) used as an emulsifier. After continuous stirring and ultrasonication, the originally transparent mixture became turbid (Supplementary Fig. 1). Further observation with optical microscopy revealed well-dispersed spherical nanodroplets, or nanovehicles, in the as-prepared nanoemulsion (Supplementary Fig. 2). Dynamic light scattering showed that the sizes of nanovehicles were approximately 400 nm (Fig. 2a) and were consistent with values reported in the literature[26,27]. Increasing the oil concentration while keeping the SDS emulsifier the same resulted in slightly larger droplets and more oil droplets per volume of dispersion (Supplementary Table 1).

We conducted a molecular dynamics (MD) simulation to understand the distribution of SDS, oil and PIP in the nanovehicles (Fig. 2b, with constructed molecular structures shown in Supplementary Fig. 3 and assembled nanovehicle in Supplementary Fig. 4). The results from MD reveal what is expected of surfactants (SDS), that their hydrophobic tails are in the oil phase while their hydrophilic heads are in the water phase, and that their concentration peaks at the water–oil interface (Fig. 2c). At the centre of the spherical nanodroplet, the concentrations of PIP and oil reached their respective maxima, suggesting that PIP was concentrated in the nanovehicles. Further evidence using NF filtration experiments confirmed the enrichment of PIP inside the nanovehicles. Specifically, after 10 min ultrasonication the PIP/oil/SDS/water mixture was filtrated by a commercial NF270 membrane (Dow FilmTec) to remove oil droplets (Fig. 2d), and the PIP concentration in the permeate (Fig. 2e) was lower than that of the control (that is, permeate from filtering an aqueous solution of PIP with the same PIP concentration but without oil and surfactants; Supplementary Fig. 5). The PIP concentration in the nanovehicle was calculated to be 17.1 ± 0.8 wt/v% (Fig. 2f), which was nearly 85 times that for an aqueous solution of PIP (0.2 wt/v%). In contrast, the permeate from filtering the PIP/oil/water emulsion using NF had almost the same PIP concentration as that of the aqueous solution of PIP, which indicated that PIP was not concentrated in the oil phase of an oil/water mixture in the absence of SDS molecules, even though PIP is soluble in oil (Supplementary Fig. 6). In other words, SDS played a crucial role in concentrating PIP inside the nanovehicles.

Nanoemulsions were stained by fluorescein sodium (excitation wavelength = 488 nm) to probe the presence of nanoemulsions on the surface of the substrate after removing excess macroscopic droplets with a rubber roller. Using a confocal laser scanning microscopy (CLSM, FV1200, Olympus), we observed that although the excess macroscopic liquid droplets on the substrate surface were removed by the rubber roller (Supplementary Fig. 7), a thin liquid layer still remained on the wetted substrate for NE800, NE1200 and NE1600 (corresponding to the prepared nanoemulsions containing 800, 1200, and 1600 mg/L oil), probably due to the strong hydrophilicity of these substrates (Supplementary Fig. 8). The thicknesses of the liquid layers were ~30 μm, which enabled adequate storage of PIP-enriched nanoemulsions for subsequent IP. The emulsified oil droplets served as nanovehicles carrying PIP monomers to the hexane phase during IP (Fig. 1b).

https://doi.org/10.1038/s44221-022-00010-3

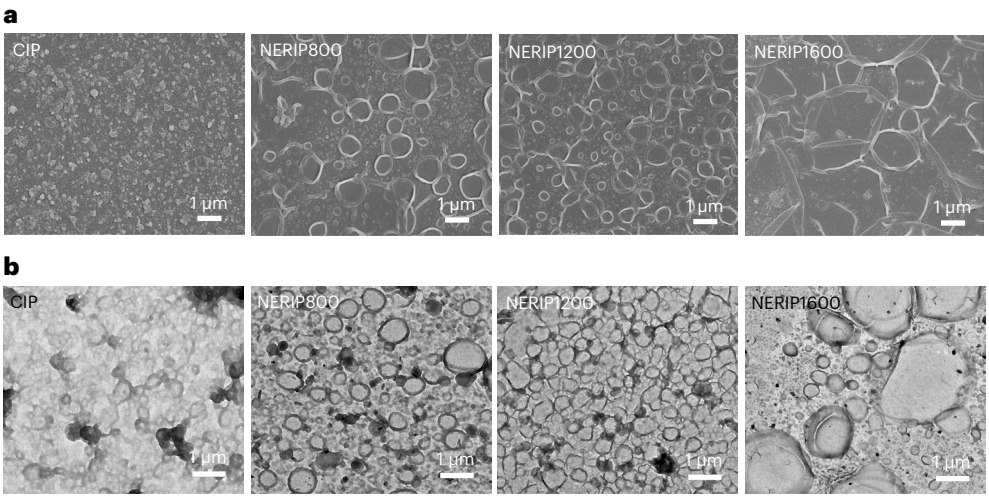

Fig. 3 | Nanocrater-like structure on PA layers resulting from nanovehicle-assisted monomer shuttling. a, SEM characterization on front surfaces of CIP and NERIP membranes. **b**, TEM projected area images of CIP and NERIP membranes. Prior to the TEM characterization, the substrates of CIP and NERIP membranes were dissolved by DMF, with pure PA layers loaded onto copper mesh.

Because oil is miscible with hexane[28,29], the oil–hexane interface disappeared upon the droplet entrance to the hexane phase, leaving a single phase (of oil and hexane) with PIP-rich spherical domains surrounded by a TMC-rich hexane medium. The polymerization reactions were then initiated at the boundary between the PIP-rich and TMC-rich domains, which resulted in PA 'bubbles' that later became nanocraters when they collapsed and merged with the PA film formed at the water–hexane interface. The abundant PIP monomers carried into the hexane phase also accelerated the polymerization reaction, which possibly facilitated the formation of a thinner and more cross-linked PA layer.

PA NF membranes with nanocrater structures fabricated from NERIP

Instead of using aqueous PIP solution as in CIP, nanoemulsion with PIP-rich nanovehicles was introduced on the polyethersulfone (PES) substrate (Supplementary Fig. 8), followed by a contact with TMC/*n*-hexane solution to initiate NERIP. The exothermic polycondensation reaction between PIP and TMC at interface generates a thin PA active layer for solute rejection[19,24] (Supplementary Fig. 9). NERIP membranes prepared using nanoemulsions of oil concentrations of 800, 1,200 and 1,600 mg l^{-1} were labelled as NERIP800, NERIP1200 and NERIP1600 NF membranes, respectively. CIP without nanovehicles was performed to fabricate the reference PA membrane (referred to as CIP membrane). Scanning electronic microscopy (SEM) and transmission electronic microscopy (TEM) characterization showed that nanocrater structures were present on the PA layer of the NERIP membranes (Fig. 3 and Supplementary Fig. 10), in contrast to the typical nodular structure observed on the surface of the CIP membrane[30]. Specifically, the NERIP1200 membrane showed the most salient nanocrater structure with an average crater diameter of ~500 nm, which corresponds well to the size of nanovehicles in the NE1200 dispersion. TEM images consistently revealed 'bubble-like' dark rings throughout the entire PA nanofilm for the NERIP membranes (Fig. 3b). Moreover, the cross-sectional TEM image (Supplementary Fig. 11) visually revealed the void domains between PA layers and substrates for NERIP membranes, while the CIP membrane presented a typical nodular structure without observable void domains (consistent with the result of projected SEM and TEM images). For NERIP membranes, the PA intrinsic thickness remained nearly constant across a nanocrater, while the PA apparent thickness depended on the height of void domain between the PA active layer and the substrate.

For the reverse osmosis membrane, the nanobubbles generated during IP between *m*-phenylenediamine (MPD) and TMC roughen the structure of the PA active layer of reverse osmosis and result in a typical ridge-valley structure that enhances the water permeance[31,32]. In contrast, conventional NF membranes prepared via IP with PIP and TMC possess a relatively smooth nodular structure due to less nanobubble generation in the relatively weaker reaction of PIP-TMC compared with MPD-TMC[22,33]. NERIP with nanovehicle-assisted monomer shuttling generated substantially different PA structure compared with CIP, and the nanocrater morphology is favourable for more efficient water transport.

To understand which component in the nanoemulsion system induced the formation of nanocrater structure, IP between an aqueous solution of PIP with SDS (but without oil) and a hexane solution of TMC was conducted. The surface of the as-formed SDS membrane was smooth (Supplementary Fig. 12), suggesting that the nanovehicles in the nanoemulsion rather than the SDS were responsible for formation of the nanocrater structure. The nanovehicles enriched in PIP merged into the hexane phase and accelerated the IP reaction, generating nanocrater structures resulting from collapsed PA 'bubbles'. Nevertheless, the fundamental relationship between the size of the nanovehicles and the nanocrater structure of the NF membranes requires further investigation.

Topographical analysis based on atomic force microscope (AFM) images confirmed the larger roughness of the NERIP membranes as compared with the reference CIP membrane (Fig. 4a). Specifically, the average height of the nodular structure was ~45 nm for the CIP membrane, whereas that of the nanocrater structures was ~150 nm for NERIP800 and NERIP1200 membranes (Fig. 4b). The reduced height of the nanocrater structure for NERIP1600 is probably due to the coalesce of nanovehicles to form patchy oil films on the PES substrate.

The surface area ratio of NERIP membranes was increased compared with that of the CIP membrane (Fig. 4c), which could contribute to more permeable sites on the surface of the PA layers from NERIP and thus faster water transport. Quartz crystal microbalance (QCM) analysis was performed to determine the void domain fraction of CIP and NERIP PA nanofilms[34]. The void domain fraction of the NERIP1200 membrane is 33.16 ± 1.38% (Fig. 4d), which is nearly 3.5 times that of the CIP membrane (9.32 ± 0.85%). The void domain fraction of the PA active layer of the NERIP1200 NF membrane was even higher than those of typical reverse osmosis membranes with ridge-valley morphologies

https://doi.org/10.1038/s44221-022-00010-3

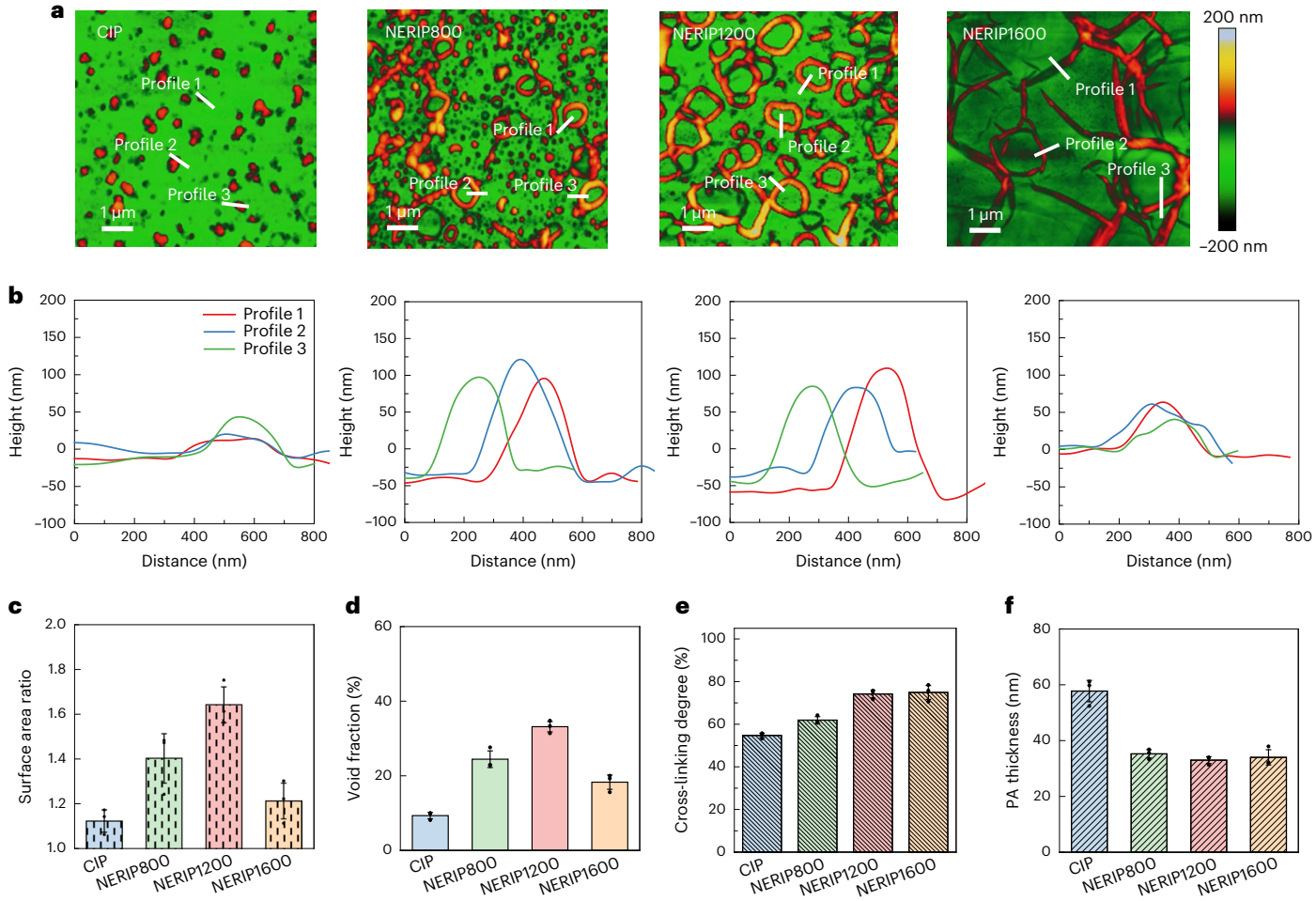

Fig. 4 | Characterization of CIP and NERIP membranes. a, A series of AFM topography images reveal the nanocrater structure for NERIP membranes, compared with a CIP membrane. The scale bar of the AFM images ranges from −200 nm to 200 nm. **b**, Height profiles of the surface of CIP and NERIP membranes. Profiles 1, 2, and 3 result from the respective white lines of height scanning in **a. c**, Surface area ratio of PA layers determined by AFM. **d**, Fraction of void domain inside PA layers determined by QCM analysis**. e**, Cross-linking degrees of PA layers calculated from XPS spectra. **f**, Thickness of PA layers measured by AFM scanning. The thickness of the PA active layer was determined by scanning the border region between the PA film and the silicon wafer. Prior to AFM height scanning, multiple parallel dents were carefully scratched on the isolated PA films (the substrates were dissolved by DMF) using a needle without damaging the silicon wafer. Error bars in **d**–f represent the s.d. ($n = 3$) and data are presented as mean values ± s.d.

(15–32%)[34]. These internal voids are liquid-filled under NF conditions and can dramatically improve water permeance[35]. The increased void fraction for the NERIP membrane was also confirmed by positron annihilation–doppler broadening energy spectroscopy (DBES). The value of the *S* parameter (the fraction of the positrons that annihilate with low-momentum valence electrons or from positronium in the membrane coupon) is generally related to the volume of voids in the PA nanofilm[36,37], that is, a larger *S* value represents a larger void fraction. Considering the thickness of the PA layer to be ~30–60 nm (shown in the following results), the positron energy range of ~0–1 keV was selected for comparison of void fractions between CIP and NERIP PA nanofilms. Consistent with the results of the QCM analysis, the NERIP PA nanofilm possessed higher void fractions than the CIP membrane (Supplementary Fig. 13).

The cross-linking degrees of the PA nanofilm, calculated from X-ray photoelectron spectroscopy (XPS) spectra (Supplementary Fig. 14, Supplementary Fig. 15 and Supplementary Table 2), increased for NERIP membranes (Fig. 4e). The increased cross-linking degree led to a lower density of carboxyl group on the PA nanofilm, inducing less negative zeta potentials at neutral pH for NERIP membranes in comparison with that of CIP membrane (Supplementary Fig. 16). We further measured the intrinsic thickness of the standalone PA nanofilms (obtained by dissolving PES) by scanning across the edge of the films (Supplementary Fig. 17) and found that all NERIP membranes have thinner PA active layers (~30 nm) compared with that of the CIP membrane (~60 nm) (Fig. 4f). The reduced intrinsic PA thickness probably results from a high cross-linking degree, as IP is a self-limiting reaction[38] in which a denser PA structure further inhibits monomer diffusion and leads to earlier termination of IP.

NF performance of NERIP membranes with nanocrater structure

The pure water fluxes of CIP and NERIP membranes linearly increased with the applied pressure ranging from 1 to 7 bar (Supplementary Fig. 18), indicating nearly constant pure water permeances of CIP and NERIP membranes within such a pressure range. Both pure water permeance and Na_2SO_4 rejection of the NERIP membranes were higher than those of the CIP membrane (Fig. 5a). For example, the NERIP1200 membrane has a pure water permeance of 36.8 ± 1.9 l m^{-2} h^{-1} bar^{-1}, which is nearly three times that of the CIP membrane. This enhancement could be attributed to increased surface area and void fraction, as well as the reduced intrinsic thickness, of the PA nanofilm with nanocrater structure.

https://doi.org/10.1038/s44221-022-00010-3

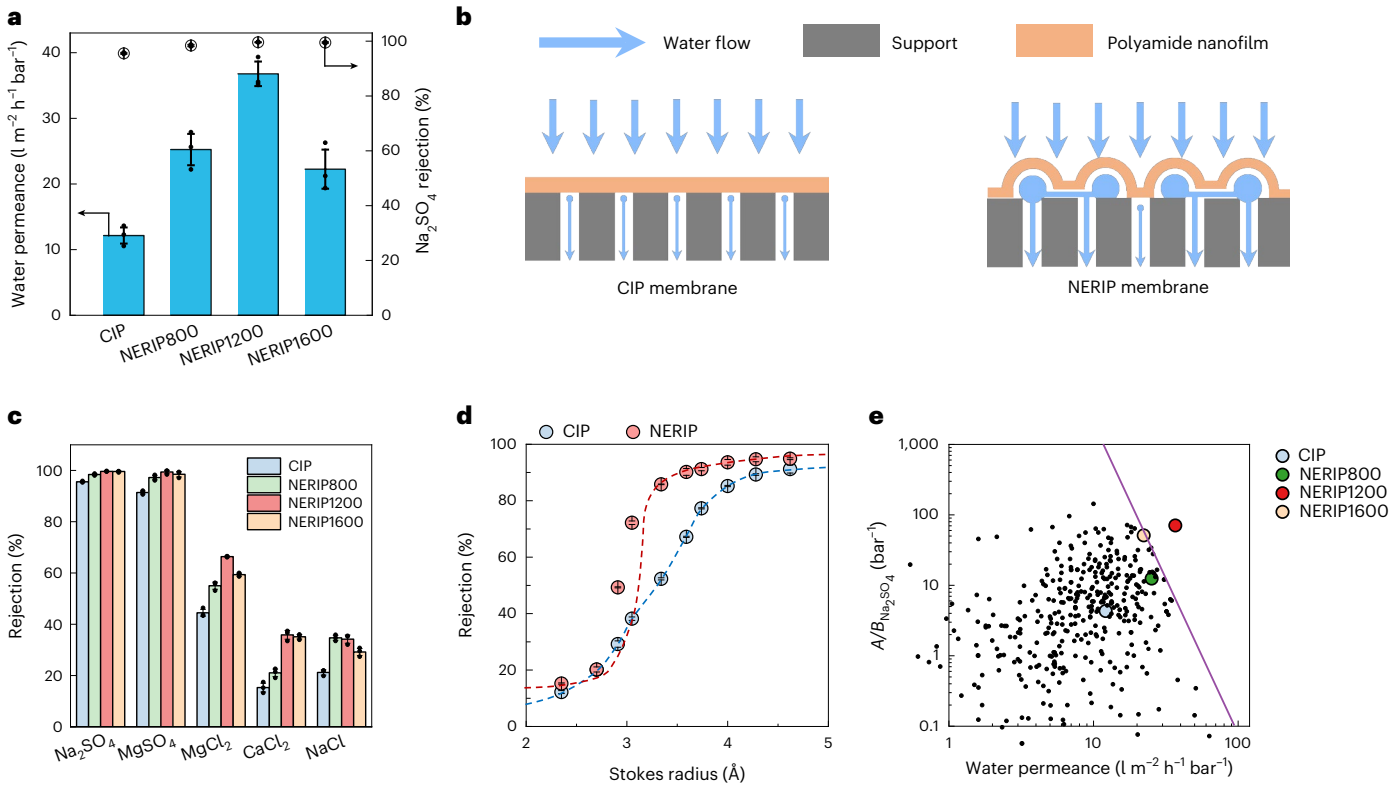

Fig. 5 | Water purification performance of PA NF membranes. a, Water permeance and Na_2SO_4 rejection of CIP and NERIP membranes. Salt concentration, 1 g l^{-1}; applied pressure, 5 bar; temperature, 25 °C. **b**, Schematic diagrams of water transport across CIP and NERIP membranes. Compared with the CIP membrane, the NERIP membrane, which has a nanocrater structure, possessed more void domain in the PA active layer, providing more permeable sites for water transport. **c**, Rejection of Na_2SO_4, $MgSO_4$, $MgCl_2$, $CaCl_2$ and NaCl by CIP and NERIP membranes. Salt concentration, 1 g l^{-1}; applied pressure, 5 bar; temperature, 25 °C. **d**, Rejection of various neutral solutes as a function of the Stokes radius for CIP and NERIP1200 membranes. **e**, Summary of water/Na_2SO_4 selectivity and water permeance of the state-of-the-art NF membranes reported in the literature. Error bars in **a** and **c** represent the s.d. ($n = 3$) and data are presented as mean values ± s.d.

Moreover, the NERIP1200 membrane also showed an improved Na_2SO_4 rejection of 99.6 ± 0.1%, higher than that of the CIP membrane (95.6 ± 0.2%). After accounting for the different degrees of concentration polarization (Supplementary Table 3), the NERIP membranes still have higher intrinsic Na_2SO_4 rejection than the CIP membrane.

We calculated the intrinsic water permeability of the CIP and NERIP membranes based on the intrinsic thickness and surface area ratio. Interestingly, NERIP membranes have higher intrinsic water permeability than that of the CIP membrane (Supplementary Table 4), which appears to contradict the higher degree of cross-linking in NERIP membranes[39]. Such a contradiction may be reconciled by considering the reduced adhesion of PA layer to PES substrate (Supplementary Fig. 11), afforded by larger void domains of the NERIP membranes (Fig. 5b): as the PES support layer has a relatively low porosity, exposing the pores of the support layer to the void domains instead of directly to the PA polymer promotes faster water transport[34,40]. It may be argued that the higher surface roughness, as one of the reasons for the higher flux, may lead to a higher fouling propensity. However, the impact of PA roughness at nanoscale on membrane fouling is still controversial in membrane communities[41–43].

The negatively charged CIP membrane showed greater rejection of Na_2SO_4 than $MgSO_4$ and greater rejection of NaCl than $CaCl_2$ (Fig. 5c) because (1) the Donnan effect with a negatively charged membrane (Supplementary Fig. 16) favours permeation of divalent cations over monovalent cations[44,45], and (2) the pore size of the CIP membrane is not sufficiently small for high divalent cation rejection via steric exclusion as the primary rejection mechanism (Supplementary Fig. 19). The NERIP1200 membrane showed increased rejection of all tested salts compared with that of the CIP membrane, which was due to smaller pores and improved steric exclusion (we note that NERIP membranes have a higher rejection of SO_4^{2-} despite a less negative zeta potential)[46,47]. The separation performance of the NERIP membranes was also evaluated using a mixture of Na_2SO_4 and NaCl (Supplementary Fig. 20). The rejections of SO_4^{2-} by the CIP and NERIP membranes slightly decreased in the presence of NaCl due to reduced Donnan exclusion (Fig. 5a). Nevertheless, the rejections of SO_4^{2-} and Cl^- in the mixture of Na_2SO_4 and NaCl by the NERIP membranes were still higher than the respective values of the CIP membrane.

The CIP membrane had a wide range of rejection for neutral solutes with a Stokes radius between 2.4 and 3.9 Å (Fig. 5d and Supplementary Table 5). In contrast, the rejection curve for the NERIP membrane presented a sharp, stepwise transition at a Stokes radius of ~3.0 Å. In other words, NERIP not only decreases the molecular weight cutoff but also sharpens the transition regime of the rejection curve, potentially enabling NERIP membranes for differentiating solutes with a sub-1-Å precision. The improved solute rejection performance could be ascribed to a more cross-linked PA network with more uniform pore size distribution for the NERIP1200 membrane (Supplementary Fig. 19), considering that Donnan and dielectric exclusions were negligible for neutral solutes.

The selectivity ($A/B_{Na_2SO_4}$), defined as water permeability coefficient/Na_2SO_4 permeability coefficient, of the CIP and NERIP membranes was compared with those of the state-of-the-art NF membranes reported in the literature (Fig. 5e)[9,10,48]. The comparison indicates that the NERIP1200 membrane outperformed NF membranes in the literature, that is, achieving the highest water/Na_2SO_4 selectivity for a given

permeance or the highest permeance for a given water/Na_2SO_4 selectivity, transcending the existing performance upper bound on the selectivity versus permeance plot. The outstanding water permeance of the NERIP1200 membrane resulted from the largest void domain and surface area ratio, and smallest PA thickness. Moreover, the favourable water/Na_2SO_4 selectivity of the NERIP1200 membrane was ascribed to the simultaneously improved water permeance and Na_2SO_4 rejection, which originated from the increased cross-linking degree and more uniform pore size distribution. The long-term performance of the NERIP1200 membrane was stable in continuous filtration up to 240 h with 1 g l^{-1} Na_2SO_4 feed solution and an applied pressure of 5 bar (Supplementary Fig. 21).

Conclusions

We have developed a facile and highly practical NERIP strategy using nanovehicle-assisted monomer shuttling to create a nanocrater-structured PA layer for a NF membrane, which dramatically enhanced the performance of the TFC-PA NF membrane with simultaneous improvements in water permeance as well as water/solute and solute/solute selectivity. The NERIP strategy enabled the formation of a PA layer with lower intrinsic thickness and nanocrater structures that substantially increased the surface area and voids fraction of the PA layer. Without using expensive materials or dramatically altering existing production lines, NERIP creates a new dimension of control for manipulating the morphology and performance of TFC-PA membranes.

Methods

Materials and chemicals

The ultrafiltration PES (UP020) support membrane with pore size of 9.7 ± 2.4 nm (Supplementary Fig. 8) was purchased from Microdyn-Nadir. The PES membranes were immersed in water for 24 h prior to any experiment. All working solutions were prepared using Milli-Q water throughout the study, unless otherwise stated. Solvents including dimethylformamide (DMF), hexane and ethanol were received from Sigma-Aldrich. PIP and TMC from Sigma-Aldrich were used for IP to form the PA selective layer. SDS as the surfactant was purchased from Macklin. Pure sunflower seed oil (abbreviated as oil throughout our paper) was obtained from Yu Pin King Hong Kong, which was primarily composed of 28% oleic acid and 72% linoleic acid. Inorganic salts (NaCl, $MgCl_2$, $CaCl_2$, $MgSO_4$ and Na_2SO_4) were supplied by Aladdin. Various neutral solutes were purchased from Macklin and Aladdin for probing pore size distribution of the PA active layer. The molecular weights and Stokes radius calculated by the Stokes–Einstein equation are shown in Supplementary Table 5. All chemicals were used as received.

Preparation of PIP/nanoemulsion

To prepare PIP/nanoemulsion (that is, emulsified droplets less than 1 μm), 400 mg l^{-1} SDS, 800–1,600 mg l^{-1} oil and 0.2 wt/v% PIP was dissolved in pure water. After being stirred for 5 min, the mixed solution was subjected to ultrasonication for 10 min in an ice bath. The intensity of ultrasonication was 700 W with time intervals of 10 s on and 5 s off. The prepared nanoemulsions containing 800, 1,200 and 1,600 mg l^{-1} oil were denoted as NE800, NE1200 and NE1600, respectively. Fresh nanoemulsion was immediately used for membrane fabrication or characterization.

Characterization of nanoemulsion

The micro-morphology of nanoemulsion was observed by an optical microscopy (Olympus IX71). Nanodroplet sizes and zeta potentials of prepared nanoemulsions were determined by a zetasizer (Zetasizer Nano ZS 90, Malvern Panalytical) with an effective size range of 0.6–6,000 nm. Turbidity of various nanoemulsions was determined by a Hach 2100Q portable turbidimeter.

Fabrication of CIP and NERIP membranes

For fabrication of CIP membrane, PES substrate was immersed in 0.2 wt/v% PIP/water for 2 min and excess PIP/water droplets were removed from the surface of the PES substrate. The surface of the PES substrate was further exposed to 0.16 wt/v% TMC/hexane for a 30 s CIP, to form a PA layer on the substrate. The as-prepared membrane was washed in sequence by hexane and 1:3 ethanol/water. The membrane (denoted as CIP membrane) was thermal treated by 60 °C oven for 5 min and subsequently stored in deionized water. For fabrication of the NERIP membrane, the PIP/water was replaced by PIP/nanoemulsion while other fabrication procedures were kept the same. The washing with 1:3 ethanol/water was used to remove residual oil droplets from the membranes after NERIP. The membranes fabricated based on PIP/nanoemulsion of 800, 1,200 and 1,600 mg l^{-1} oil were denoted as NERIP800, NERIP1200 and NERIP1600 membranes, respectively.

Membrane characterization

SEM characterization on membranes was conducted by a field emission scanning electron microscope (FESEM, ZEISS GEMINI SEM 300) at 5.0 kV. Before SEM characterization, membranes were dried at 40 °C oven and sputtered with platinum and gold for enhancing surface conductivity. To obtain an isolated PA active layer, the CIP or NERIP membranes were dried first and immersed in the pure DMF for dissolution of PES substrates. The isolated PA active layer was transferred to copper mesh for TEM characterization, and the PA layer was also transferred onto silicon wafer for back-surface SEM observation and AFM height scanning. A TEM (Philips CM100) was used for obtaining transmission images of isolated PA layers at an accelerating voltage of 100 kV. Membrane surface roughness and the thickness of the PA active layer were analysed by an AFM (Veeco NanoScope MultiMode III) in peak force tapping mode. For surface roughness measurement, the PA active layer was dried and subjected to AFM scanning. The thickness of the PA active layer was determined by scanning the border region between the PA film and the silicon wafer. Prior to AFM height scanning, multiple parallel dents were carefully scratched on the isolated PA films using a needle without damaging the silicon wafer. AFM images were all processed using Nanoscope Analysis software. An electrokinetic analyser (SurPASS 3, Anton Paar) was applied to determine zeta potentials of the surface of various membranes at various pH values. The surface compositions of CIP and NERIP membranes were characterized by XPS (PHI 5000 C ESCA System).

Calculation of cross-linking degree of membranes

Based on the O/N elemental ratio from the XPS spectra, we calculated the degree of cross-linking of the PA active layers. The cross-linking degree refers to the proportion of the fully cross-linked structure in the PA layer, which indicates that each acid chloride group (Cl–C = O) of TMC is bonded to the $-NH_2$ group of an amine monomer forming an amide structure. The remaining proportion suggests the fully linear structure in which one chloride group of TMC remains unreacted and is finally hydrolysed to form a carboxylic acid. The following equation was used to calculate the cross-linking degree:

$$\frac{O}{N} = \frac{3m + 4n}{3m + 2n}, m + n = 1 \quad (1)$$

where m and n are the cross-linking portion and linear portion, respectively. The cross-linking degree is then obtained by $m \times 100\%$.

Determination of voids fraction in PA active layer by QCM

A QCM (Q-sense E4, Biolin Scientific) was used to quantify the void domain in the PA nanofilms. The PES substrates of the NERIP membranes were dissolved by DMF and the resultant isolated PA active layers were transferred onto QCM gold sensors (QSX301, Q-sense). The areal mass of active layers (m^0_{AL}, ng cm^{-2}) was obtained from the difference in QCM responses between the coated and uncoated sensors when being exposed to dry nitrogen gas. The areal mass of water absorbed by active

layers (m^{w}_{AL}, ng cm^{-2}) was obtained from the difference in QCM responses for the coated sensor between exposure to ultrapure water and to dry nitrogen. Those measurements were conducted by a Q-sense flow module (QFM401, Biolin Scientific) with the water flow rate of 0.14 ml min^{-1}. The sensor response was monitored until the system reached equilibrium (>1 h). A Q-sense humidity module (QHM401, Biolin Scientific) was then employed to measure the areal mass of water absorbed by active layers after exposure to nitrogen gas at 94% relative humidity (m^{w}_{ALO}, ng cm^{-2}), which represented the water uptake by the active layer polymer itself (excluding the water contained by pores). For comparison, the m^{w}_{AL} calculated the water uptake by the whole active layer (including pores). During the measurement, the water flow rate was 0.08 ml min^{-1}. The void domain fraction (f_{void}, %) of PA active layers was calculated based on m^{0}_{AL}, m^{w}_{AL} and m^{w}_{ALO} according to the following equation[34]:

$$f_{void} = \frac{\text{Pore volume}}{\text{Active layer volume+Pore volume}} = \frac{(m^{w}_{AL} - m^{w}_{ALO})/\rho_w}{m^{0}_{AL}/\rho_{AL} + (m^{w}_{AL} - m^{w}_{ALO})/\rho_w} \times 100\% \quad (2)$$

where $\rho_w = 0.997$ g cm^{-3} corresponds to water density at 25 °C, and $\rho_{AL} = 1.240$ g cm^{-3} refers to the dry mass density of polyamide active layers.

Positron annihilation–DBES measurement

The microstructure of PA films was characterized by a positron annihilation coupled DBES (Institute of High Energy Physics, Beijing, China) using ^{22}Na radioactive source as the positron source. The DBES spectra were collected at different incident energies between 0 and 10 keV. The *S* parameter of DBES was calculated from the ortho-positronium 2 g pick-off annihilation in free volume, reflecting the depth profile information of the free volume (Å to nm) in the PA nanofilm. The mean implantation depth of positron in the PA films was calculated by the following equation:

$$Z(E_+) = \left(\frac{40}{\rho}\right) E_+^{1.6} \quad (3)$$

where Z is the mean implantation depth in the PA film (nm), ρ is the density of polymer materials (1.25 g cm^{-3} for PA) and E_+ represents the incident positron energy in keV.

Membrane performance test

The NF performance of CIP and NERIP membranes was evaluated in a lab-scale cross-flow membrane filtration setup[22,23,49]. A membrane coupon (9.1 cm^2) was pre-compacted at an applied pressure of 6 bar with a cross-flow velocity of 20.0 cm s^{-1} for 4 h to stabilize the permeate flux. The temperature of feed solution was kept constant at 25.0 ± 0.5 °C. The water flux and rejection rate of salts and neutral solutes were measured at 5 bar. The salt concentration in the feed solution was 1,000 mg l^{-1} and the concentration of neutral solute was 40 mg l^{-1} (in total organic carbon). The salt concentration in the feed or permeate was determined by a conductivity meter, while the concentrations of neutral solutes were quantified by a total organic carbon analyser. The water flux J_w was determined by the following equation:

$$J_w = \frac{\Delta w}{\rho A \Delta t} \quad (4)$$

where Δw is the weight change of permeate during filtration time Δt, A is the effective area of each cross-flow cell and ρ is the density of the permeate. The rejection of salts and neutral solutes (R) was calculated by the following equation based on the concentration of the feed (C_f) and permeate (C_p) solutions:

$$R = \left(1 - \frac{C_p}{C_f}\right) \times 100\% \quad (5)$$

Water permeance refers to the water flux per unit applied pressure, as shown in the following equation, where ΔP is the applied pressure in the cross-flow filtration experiment:

$$\text{Water permeance} = \frac{J_w}{\Delta P} \quad (6)$$

MD simulation

MD simulation was conducted to provide an atom-level insight of the structure transformation of a mixed solution (consisting of oil (oleic acid and linoleic acid), PIP, SDS and water), and the diffusion process of PIP at different systems. The molecular structures of PIP, oil, SDS and water molecules are shown in Supplementary Fig. 4. For the structure transformation simulation, the simulation system consisted of 64 oleic acid molecules, 160 linoleic acid molecules, 1,160 PIP molecules, 70 SDS molecules and 6,000 water molecules. The initial configuration of the system was constructed through the software PACKMOL[50] and all the molecules were randomly inserted in a cubic simulation box. The GROMOS 54A7 force field[51] was employed to describe the behaviour of the molecules. The molecular force field consists of non-bonded and bonded interaction. The non-bonded interaction contains van der Waals (E_{LJ}) and electrostatic interaction (E_c), which is described by equations (7) and (8), respectively:

$$E_{LJ}(r_{ij}) = 4\varepsilon_{ij}\left(\left(\frac{\sigma_{ij}}{r_{ij}}\right)^{12} - \left(\frac{\sigma_{ij}}{r_{ij}}\right)^{6}\right) \quad (7)$$

$$E_c(r_{ij}) = \frac{q_i q_j}{4\pi\varepsilon_o\varepsilon_r r_{ij}} \quad (8)$$

where r_{ij} is the distance between particles; ε_{ij} is the potential well depth; σ_{ij} is the distance at which the intermolecular potential between the two particles is zero; q_i/q_j refers to the electric charge of particle i/j; ε_o is the dielectric constant; ε_r is the relative dielectric constant. For different kinds of atoms, the Lorentz–Berthelot mixing rules were adopted for van der Waals interactions following equation (9). The cutoff distance of van der Waals and electronic interactions was set to 1.2 nm, and the particle mesh Ewald method was employed to calculate long-range electrostatic interactions.

$$\sigma_{ij} = \frac{1}{2}(\sigma_{ii} + \sigma_{jj}); \varepsilon_{ij} = (\varepsilon_{ii} \times \varepsilon_{jj})^{1/2} \quad (9)$$

in which σ_{ii}, σ_{jj} loosely reflect the radii of particles i and j, respectively; ε_{ii}, ε_{jj} are instantaneous dipoles of particles i and j, respectively. For the structure transformation simulation, an energy minimization was firstly used to relax the simulation box. Then, an isothermal–isobaric (NPT) ensemble with a 1.0 fs time step was employed to simulate the process of structure transformation. The pressure of both systems was set to 1.0 atm, which was kept via the Parrinello–Rahman barostat. The temperature was 298.15 K, which was kept via the Nose–Hoover thermostat barostat. The NPT optimization time was 5.0 ns, which is long enough to obtain a stable box size. Following the NPT simulation, a canonical (NVT) ensemble with 80.0 ns was performed to collect the trajectory coordinates of molecules with a storage frequency of 1,000 steps. The time step of NVT simulation was set to 1.0 fs. In all the MD simulations, the motion of atoms was described by classical Newton's equation, which was solved using the velocity Verlet algorithm. All simulations were performed using the GROMACS 2019.5 package[52].

Data availability

All relevant data that support the findings of this study are presented in the Article and Supplementary Information. Source data are provided

with this paper. The source data can also be accessed through the figshare repository and are freely available for download.

Code availability

The codes for the MD simulation performed are provided with this paper. The initial configuration for the mixture box of MD simulation was built from the PACKMOL package. GROMACS was used to input files of GROMACS package of MD simulation including EM (energy minimization), NPT (isothermal–isobaric ensemble) and NVT (canonical ensemble). Data analysis was conducted by using the processing code for number density along the *z* axis.

References

1. Elimelech, M. & Phillip, W. A. The future of seawater desalination: energy, technology, and the environment. *Science* **333**, 712–717 (2011).
2. Werber, J. R., Osuji, C. O. & Elimelech, M. Materials for next-generation desalination and water purification membranes. *Nat. Rev. Mater.* **1**, 16018 (2016).
3. Ritt, C. L. et al. Machine learning reveals key ion selectivity mechanisms in polymeric membranes with subnanometer pores. *Sci. Adv.* **8**, eabl5771 (2022).
4. Petersen, R. J. Composite reverse osmosis and nanofiltration membranes. *J. Membr. Sci.* **83**, 81–150 (1993).
5. Hilal, N., Al-Zoubi, H., Darwish, N. A., Mohamma, A. W. & Abu Arabi, M. A comprehensive review of nanofiltration membranes: treatment, pretreatment, modelling, and atomic force microscopy. *Desalination* **170**, 281–308 (2004).
6. Logan, B. E. & Elimelech, M. Membrane-based processes for sustainable power generation using water. *Nature* **488**, 313–319 (2012).
7. Culp, T. E. et al. Nanoscale control of internal inhomogeneity enhances water transport in desalination membranes. *Science* **371**, 72–75 (2021).
8. Guo, H. et al. Tweak in puzzle: tailoring membrane chemistry and structure toward targeted removal of organic micropollutants for water reuse. *Environ. Sci. Technol. Lett.* **9**, 247–257 (2022).
9. Yang, Z., Long, L., Wu, C. & Tang, C. Y. High permeance or high selectivity? Optimization of system-scale nanofiltration performance constrained by the upper bound. ACS EST Eng. (2021).
10. Yang, Z., Guo, H. & Tang, C. Y. The upper bound of thin-film composite (TFC) polyamide membranes for desalination. *J. Membr. Sci.* **590**, 117297 (2019).
11. Zhao, Y. et al. Differentiating solutes with precise nanofiltration for next generation environmental separations: a review. Environ. Sci. Technol. (2021).
12. Saha, N. K. & Joshi, S. V. Performance evaluation of thin film composite polyamide nanofiltration membrane with variation in monomer type. *J. Membr. Sci.* **342**, 60–69 (2009).
13. Chowdhury, M. R., Steffes, J., Huey, B. D. & McCutcheon, J. R. 3D printed polyamide membranes for desalination. *Science* **361**, 682–686 (2018).
14. Jiang, Z., Karan, S. & Livingston, A. G. Water transport through ultrathin polyamide nanofilms used for reverse osmosis. *Adv. Mater.* **30**, 1705973 (2018).
15. Sarkar, P., Modak, S. & Karan, S. Ultraselective and highly permeable polyamide nanofilms for ionic and molecular nanofiltration. *Adv. Funct. Mater.* **31**, 2007054 (2021).
16. Park, H. B., Kamcev, J., Robeson, L. M., Elimelech, M. & Freeman, B. D. Maximizing the right stuff: the trade-off between membrane permeability and selectivity. *Science* **356**, eaab0530 (2017).
17. Werber, J. R., Deshmukh, A. & Elimelech, M. The critical need for increased selectivity, not increased water permeability, for desalination membranes. *Environ. Sci. Technol. Lett.* **3**, 112–120 (2016).
18. Epsztein, R., DuChanois, R. M., Ritt, C. L., Noy, A. & Elimelech, M. Towards single-species selectivity of membranes with subnanometre pores. *Nat. Nanotechnol.* **15**, 426–436 (2020).
19. Tan, Z., Chen, S., Peng, X., Zhang, L. & Gao, C. Polyamide membranes with nanoscale Turing structures for water purification. *Science* **360**, 518–521 (2018).
20. Wang, Z. et al. Nanoparticle-templated nanofiltration membranes for ultrahigh performance desalination. *Nat. Commun.* **9**, 2004 (2018).
21. Liang, Y. et al. Polyamide nanofiltration membrane with highly uniform sub-nanometre pores for sub-1 Å precision separation. *Nat. Commun.* **11**, 2015 (2020).
22. Dai, R. et al. Hydrophilic selective nanochannels created by metal organic frameworks in nanofiltration membranes enhance rejection of hydrophobic endocrine-disrupting compounds. *Environ. Sci. Technol.* **53**, 13776–13783 (2019).
23. Dai, R., Wang, X., Tang, C. Y. & Wang, Z. Dually charged MOF-based thin-film nanocomposite nanofiltration membrane for enhanced removal of charged pharmaceutically active compounds. *Environ. Sci. Technol.* **54**, 7619–7628 (2020).
24. Karan, S., Jiang, Z. & Livingston, A. G. Sub-10 nm polyamide nanofilms with ultrafast solvent transport for molecular separation. *Science* **348**, 1347–1351 (2015).
25. Yuan, B., Zhao, S., Hu, P., Cui, J. & Niu, Q. J. Asymmetric polyamide nanofilms with highly ordered nanovoids for water purification. *Nat. Commun.* **11**, 6102 (2020).
26. Qin, D., Liu, Z., Bai, H., Sun, D. D. & Song, X. A new nano-engineered hierarchical membrane for concurrent removal of surfactant and oil from oil-in-water nanoemulsion. *Sci. Rep.* **6**, 24365 (2016).
27. Artiga-Artigas, M., Guerra-Rosas, M. I., Morales-Castro, J., Salvia-Trujillo, L. & Martín-Belloso, O. Influence of essential oils and pectin on nanoemulsion formulation: a ternary phase experimental approach. *Food Hydrocoll.* **81**, 209–219 (2018).
28. Kaparthi, R. & Chari, K. S. Solubilities of vegetable oils in aqueous ethanol and ethanol-hexane mixtures. *J. Am. Oil Chem. Soc.* **36**, 77–80 (1959).
29. Friedrich, J. P. & List, G. R. Characterization of soybean oil extracted by supercritical carbon dioxide and hexane. *J. Agric. Food Chem.* **30**, 192–193 (1982).
30. Lu, Y. et al. Two-dimensional fractal nanocrystals templating for substantial performance enhancement of polyamide nanofiltration membrane. *Proc. Natl Acad. Sci. USA* **118**, e2019891118 (2021).
31. Ma, X.-H. et al. Nanofoaming of polyamide desalination membranes to tune permeability and selectivity. *Environ. Sci. Technol. Lett.* **5**, 123–130 (2018).
32. Song, X., Gan, B., Yang, Z., Tang, C. Y. & Gao, C. Confined nanobubbles shape the surface roughness structures of thin film composite polyamide desalination membranes. *J. Membr. Sci.* **582**, 342–349 (2019).
33. Dai, R., Han, H., Zhu, Y., Wang, X. & Wang, Z. Tuning the primary selective nanochannels of MOF thin-film nanocomposite nanofiltration membranes for efficient removal of hydrophobic endocrine disrupting compounds. *Front. Environ. Sci. Eng.* **16**, 40 (2021).
34. Lin, L., Lopez, R., Ramon, G. Z. & Coronell, O. Investigating the void structure of the polyamide active layers of thin-film composite membranes. *J. Membr. Sci.* **497**, 365–376 (2016).
35. Wong, M. C. Y., Lin, L., Coronell, O., Hoek, E. M. V. & Ramon, G. Z. Impact of liquid-filled voids within the active layer on transport through thin-film composite membranes. *J. Membr. Sci.* **500**, 124–135 (2016).

36. He, Y., Tang, Y. P. & Chung, T. S. Concurrent removal of selenium and arsenic from water using polyhedral oligomeric silsesquioxane (POSS)–polyamide thin-film nanocomposite nanofiltration membranes. *Ind. Eng. Chem. Res.* **55**, 12929–12938 (2016).
37. Gan, B. et al. Ultrathin polyamide nanofilm with an asymmetrical structure: a novel strategy to boost the permeance of reverse osmosis membranes. *J. Membr. Sci.* **612**, 118402 (2020).
38. Freger, V. & Ramon, G. Z. Polyamide desalination membranes: formation, structure, and properties. *Prog. Polym. Sci.* **122**, 101451 (2021).
39. Wen, Y. et al. Metal-organic framework enables ultraselective polyamide membrane for desalination and water reuse. *Sci. Adv.* **8**, eabm4149 (2022).
40. Peng, L. E. et al. A critical review on porous substrates of TFC polyamide membranes: mechanisms, membrane performances, and future perspectives. *J. Membr. Sci.* **641**, 119871 (2022).
41. Jiang, Z., Karan, S. & Livingston, A. G. Membrane fouling: does microscale roughness matter? *Ind. Eng. Chem. Res.* **59**, 5424–5431 (2020).
42. Shang, C., Pranantyo, D. & Zhang, S. Understanding the roughness–fouling relationship in reverse osmosis: mechanism and implications. *Environ. Sci. Technol.* **54**, 5288–5296 (2020).
43. Guo, W., Ngo, H.-H. & Li, J. A mini-review on membrane fouling. *Bioresour. Technol.* **122**, 27–34 (2012).
44. Luo, J. & Wan, Y. Effects of pH and salt on nanofiltration—a critical review. *J. Membr. Sci.* **438**, 18–28 (2013).
45. Szoke, S., Patzay, G. & Weiser, L. Characteristics of thin-film nanofiltration membranes at various pH-values. *Desalination* **151**, 123–129 (2003).
46. Epsztein, R., Shaulsky, E., Dizge, N., Warsinger, D. M. & Elimelech, M. Role of ionic charge density in Donnan exclusion of monovalent anions by nanofiltration. *Environ. Sci. Technol.* **52**, 4108–4116 (2018).
47. Boo, C. et al. High performance nanofiltration membrane for effective removal of perfluoroalkyl substances at high water recovery. *Environ. Sci. Technol.* **52**, 7279–7288 (2018).
48. Ritt, C. L. et al. The open membrane database: synthesis–structure–performance relationships of reverse osmosis membranes. *J. Membr. Sci.* **641**, 119927 (2022).
49. Dai, R. et al. Fouling is the beginning: upcycling biopolymer-fouled substrates for fabricating high-permeance thin-film composite polyamide membranes. *Green Chem.* **23**, 1013–1025 (2021).
50. Martínez, L., Andrade, R., Birgin, E. G. & Martínez, J. M. PACKMOL: a package for building initial configurations for molecular dynamics simulations. *J. Comput. Chem.* **30**, 2157–2164 (2009).
51. Schmid, N. et al. Definition and testing of the GROMOS force-field versions 54A7 and 54B7. *Eur. Biophys. J.* **40**, 843–856 (2011).
52. Páll, S., Abraham, M. J., Kutzner, C., Hess, B. & Lindahl, E. in *Solving Software Challenges for Exascale* (eds Markidis, S. & Laure, E.) 3–27 (Springer, 2015).

Acknowledgements

We thank the National Natural Science Foundation of China (51925806 (Z.W.), 51838009 (Z.W.), 52200108 (R.D.)), the US National Science Foundation (2017998 (S.L.)) and the Shanghai Sailing Program (22YF1450700 (R.D.)) for financial support.

Author contributions

R.D., S.L., C.Y.T. and Z.W. conceived the idea and designed the research. R.D., H.Z., T.W., Z.Q. and L.L. performed the experiment including nanoemulsion preparation, simulation, membrane fabrication, characterization and performance test. S.L. and C.Y.T. provided constructive suggestions for the results and discussion. R.D., S.L., C.Y.T. and Z.W. contributed to writing the manuscript. All co-authors discussed the results.

Competing interests

The authors declare no competing interests.

Additional information

Supplementary information The online version contains supplementary material available at https://doi.org/10.1038/s44221-022-00010-3.

Correspondence and requests for materials should be addressed to Shihong Lin, Chuyang Y. Tang or Zhiwei Wang.

Peer review information *Nature Water* thanks the anonymous reviewers for their contribution to the peer review of this work.